Journal of
Materials Chemistry A

Accepted Manuscript

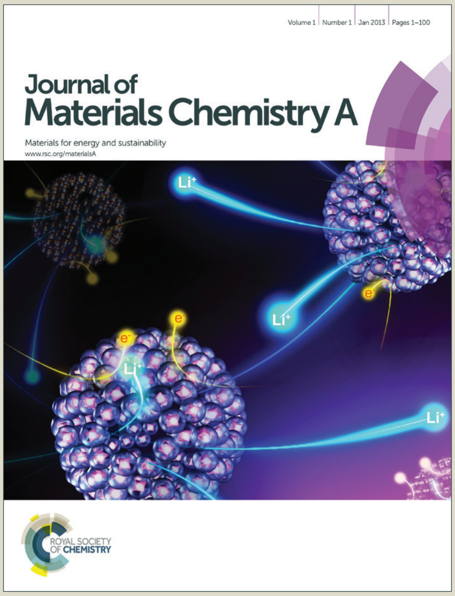

ROYAL SOCIETY
OF **CHEMISTRY**

www.rsc.org/materialsA

Paper REVISED as a *full paper* for submission to ***J. Mat. Chem. A***

Novel Au/Pd@Carbon Macrocellular Foams as Electrodes for Lithium-Sulfur Batteries

Martin Depardieu,[1,3] Raphaël Janot,[2] Clément Sanchez,[3] Ahmed Bentaleb,[1]

Rezan Demir-Cakan,[2,†] Christel Gervais,[3] Marc Birot,[4]

Mathieu Morcrette[2,*] and Rénal Backov[1,*]

[1] Université de Bordeaux, Centre de Recherche Paul Pascal, UPR 8641 CNRS, 115 Avenue Albert Schweitzer, 33600 Pessac, France.

Email: backov@crpp-bordeaux.cnrs.fr

[2] Laboratoire de Réactivité et Chimie des Solides, UMR 6007 CNRS, Université de Picardie Jules Verne, 33 Rue Saint Leu, 80039 Amiens, France.

Email: mathieu.morcrette@u-picardie.fr

[3] Sorbonne Universités, UPMC Univ Paris 06, CNRS, Collège de France, UMR 7574, Chimie de la Matière Condensée de Paris, F-75005, Paris, France.

[4] Université de Bordeaux, Institut des Sciences Moléculaires, UMR 5255 CNRS, 351 cours de la Libération, 33405 Talence, France.

† Present address: Gebze Institute of Technology, Gebze, Turkey.

Abstract

Macro-mesocellular carbonaceous foams bearing metallic (Pd or Au) nanoparticles have been synthesized and used to confine polysulfides at the cathode of Li-S batteries. We show that noble metal nanoparticles are interesting to tune the properties of cathode materials. On one hand, the surface chemistry of the metals enhances the polysulfides anchoring strength involved in carbon-based Li-S electrodes cycling batteries. On the other hand, the metallic nanoparticles nucleation and growth decreases the carbonaceous foams mesoporosity appearing, at first glance, as a penalty. The Au@C-HIPE$_{(80HF)}$ sample shows a capacity for the first discharge at 327 mA.h.cm^{-3} decreasing to 182 mA.h.cm^{-3} after 50 cycles, corresponding respectively to 430 and 240 mA.h.g^{-1}. The most efficient sample in term of power density per mass, C-HIPE$_{(2P5HF)}$, exhibits a capacity for the first discharge at 202 mA.h.cm^{-3} decreasing to 150 mA.h.cm^{-3} after 50 cycles (respectively 1680 and 1000 mA.h.g^{-1}). Hence, considering the capacity retention, the most interesting sample (C-HIPE$_{(2P5HF)}$), if power density per weight is taken as the main criteria of choice, becomes one of the less efficient if we consider power density per volume. This work demonstrates further the importance of normalizing the power density not only by weight (mA.h.g^{-1}) but also by volume (mA.h.cm^{-3}) in order to provide absolute and comparable energy storage capabilities from one sample to another.

Keywords: Porous carbon; HIPE; Li-Sulfide battery; Integrative chemistry; Energy

Introduction

Due to the exponential increase of earth population and associated decrease of the petroleum reserves, energy and environmental sciences are certainly the scientific domains where expectations from societal needs are the highest. With the goal of minimizing both air pollution and greenhouse gas emission, the production of electric (EVs) and hybrids (HEVs) vehicles has largely increased within the last ten years. One issue that still needs to be overcome is the low autonomy compared to conventional gas-based vehicles. There is thereby a crucial need for an efficient power source for electric engines that would reach the EV and HEV drastic targets in terms of energy density, safety and cost.[1,2] Lithium-sulfur chemistry holds great promises for EV battery applications with a theoretical capacity of 1675 $mA\cdot h\cdot g^{-1}$, nearly one magnitude higher than that of $LiFePO_4$ cathodes (theoretical capacity of 176 $mA\cdot h\cdot g^{-1}$).[3] Nevertheless, the Li/S system has not been implemented in EVs because of several difficulties that still need to be circumvented. The dissolution of sulfur that reacts with lithium metal induces a non stable insulating SEI layer made of sulfur and Li_2S irreversibly deposited both at the cathode and Li anode.[4] One way of optimizing both charge transport while constraining polysulfides at the cathode is their confinement within conductive carbonaceous porous media.[5] An original path, employing *in situ* chemically synthesized polysulfide species leading to liquid-based cathodes labeled “catholytes”, has shown to generate better performances than conventional Li-S cell configuration.[6] Particularly, the authors have addressed the key role of the strength and porosity of the carbon electrode in both the electrochemical properties and the detrimental formation of Li_2S at the porous carbon matrix. This approach has been extended in our group when conceiving rationally monolithic carbonaceous foams bearing hierarchical porosity,[7] in a study correlating the obtained capacity with the macrocellular foams porosity and surface area. The optimized carbonaceous monolithic foam was bearing the outstanding remnant capacity of around 1000 $mAhg^{-1}$ after

50 cycles. The issue of large volume change of the sulfur cathode during lithiation/delithiation in foams bearing macroporosity has also been overcome. Dealing with porous matter, we have proposed to address the capacity not only in weight dimensionality (mA.h.g^{-1}) but also in volumic one (mA.h.cm^{-3}) in order to be more consistent and comparable from one system to another while not forgetting a crucial technological and industrial parameter, namely the power density per volume.

In this context, we have prepared several carbonaceous foams bearing hierarchical porosity loaded with noble metals as gold and palladium. As said above, one penalty of the LiS electrodes is the insulating nature of sulfur and low solubility of lithium polysulfide intermediates (Li_2S_x, $4 \leq x \leq 8$). It is well know that noble metals bearing high surface energy present a strong affinity with sulfur atoms. We have recently demonstrated the preferential nucleation and growth of $Li(BH_4)$ at the metallic nanoparticle surface rather than at the carbonaceous foams surface, leading to cycling hydrogen storage properties.[8] Thereby the foams loaded with metallic nanoparticles are interesting to potentially promote polysulfides precipitation at the nanoparticles surface rather than at the carbon surface.

Experimental section

Chemicals.

Tetraethylorthosilicate ($Si(OEt)_4$, TEOS 99%); dodecane, 90%; Synperonic® P123 and Pluronic® F127 (poly(ethylene glycol)-block-poly(propylene glycol)-block-poly(ethylene glycol)); palladium chloride ($PdCl_2$), and potassium tetrachloroaurate ($KAuCl_4$) were purchased from Sigma-Aldrich. Tetradecyltrimethylammonium bromide ($C_{14}H_{29}N(CH_3)_3Br$, TTAB, 98%), was obtained from Alfa Aesar. Hydrochloric acid, 37%, was purchased from Carlo Erba Reagents. Ablaphene RS101 (formophenolic prepolymer of the resol type in a hydroalcoholic solution) was purchased from Rhodia. All chemicals were used as received without further purification.

Macrocellular silica hard template synthesis (Si-HIPE)

The synthesis of the silica hard template from the combination of sol-gel chemistry and the concentrated emulsion technique has been studied and described elsewhere.[9] Typically, TEOS (5 g) was added to an acidified TTAB solution (16 g of 35 wt % TTAB in water with 6 g HCl). The mixture was hand-stirred until it became transparent as TEOS was hydrolyzed. It was then transferred into a mortar and dodecane (35 g) was added drop by drop while stirring slowly with a pestle. After the last drop of dodecane, stirring was maintained for a few seconds to ensure the concentrated emulsion homogeneity. This emulsion was then poured into molds – in this case polystyrene test tubes – and left to rest for a week while the condensation reactions took place. At this stage, drying has to be avoided, the tubes were therefore either closed or put in a five litres dessicator under a saturated water/ethanol atmosphere obtained by placing a 100 milliliter solution of 50:50 volume percentage water/ethanol inside the dessicator. After condensation, the samples were put in a 1:1 vol./vol. THF/acetone mix three times for 24 h to eliminate dodecane. Then, they were slowly dried in a desiccator over a few days. After drying, the Si-HIPEs were calcinated at 650 °C for 6 h with a heating rate of 2 $°C \cdot min^{-1}$ and a first plateau at 200 °C for 2 h to eliminate surfactant residues.

Carbon foams synthesis (C-HIPE)

The overall foams synthetic paths have been described elsewhere.[10] Typically, Si-HIPE monoliths were immerged in a beaker containing a solution composed of: 25 wt % of phenolic resin in THF (25HF); 80 wt % of phenolic resin in THF (80HF); a 15:2:5 wt/wt mix of ethanol, P123 and phenolic resin (2P5HF); or a 15:4:5 wt/wt mix of ethanol, F127 and phenolic resin (4F5HF). The beakers were placed under dynamic vacuum until the effervescence, from the air removal from the silica foams, stopped. The system was then let under static vacuum for three days. The samples were rapidly rinsed with either THF (25HF, 80HF) or ethanol (2P5HF, 4F5HF), and then placed in an oven at 80 °C for 24 h to initiate resin polymerization. To complete the polymerization, a thermal treatment under air at 155 °C for 5 h was applied (heating rate of 2 $°C·min^{–1}$; first plateau at 80 °C for 12 h; second plateau at 110 °C for 3 h). Pyrolysis was performed under argon at 900 °C for 1 h, with a heating rate of 4 $°C·min^{–1}$. A plateau at 350 °C for 30 min was added for samples 2P5HF and 4F5HF to eliminate the copolymers before pyrolysis. Finally, silica hard template removal was realized by washing with a 10 wt % HF solution for 24 h and rinsing three times for 24 h in distilled water.

Palladium nanoparticles heterogeneous nucleation

C-HIPE foam was put in a beaker containing a 0.05 M solution of $PdCl_2$ in a 1:1 vol./vol. acetone/water mixture acidified with HCl. The beaker was put under dynamic vacuum until effervescence stopped, and then left under static vacuum for three days. The samples were dried in air, and then $PdCl_2$ was reduced by a thermal treatment at 400 °C (heating rate 2 $°C·min^{–1}$) under H_2. Four hybrid foams were synthesized Pd@C-HIPE$_{(25HF)}$, Pd@C-HIPE$_{(80HF)}$, Pd@C-HIPE$_{(2P5HF)}$ and Pd@C-HIPE$_{(4F5HF)}$.

Gold nanoparticles heterogeneous nucleation

The same procedure was used with a 0.05 M solution of $KAuCl_4$. After drying in air, $KAuCl_4$ was reduced by a thermal treatment at 80 °C under 0.8 MPa of H_2. These samples are labeled hereafter as Au@C-HIPE$_{(25HF)}$, Au@C-HIPE$_{(80HF)}$, Au@C-HIPE$_{(2P5HF)}$ and Au@C-HIPE$_{(4F5HF)}$.

Overall, the Pd and Au loaded foams are labeled hereafter as X@C-HIPE$_{(y)}$. X, being the included metallic nanoparticles type (Pd or Au), and Y being either the tensioactive molecules added to create the mesoporosity during the synthetic path (2P5 and 4F5) or the weight% of resorcinol dissolved in THF (25 or 80). HF stands for the silica dissolution once thermal treatment has been treatment.

Li-S electrode preparations.

Electrolyte solutions used in this study were 1 M LiTFSI (lithium bis(trifluoromethanesulfonyl)imide) containing tetra methylene sulphone (TMS). Li_2S_6 was chemically synthesized by reacting stoichiometric amounts of sulfur and lithium in ethylene glycol diethyl ether at 150 °C. Samples have been grind gently then put in a swagelok-type cell, with a felt buffer beween the carbon sample and the lithium sheet cathode. On this assembly was deposited the already mentioned electrolyte/solvant/Li_2S_6 solution (0.1 mL) , in which Li_2S_6 has a 0.1M concentration. The sulfur content has been adjusted to 1.92 mg for each experiment. Carbon foams (10 mg) were very smoothly grinded in order to keep the porosity without any added carbons. The counter electrode is made of pure lithium foil while the electrodes barriers being a glass fiber gf/d from Whatman. The carbon sample's thickness (around 1 mm) in the cell varies between samples as a constant mass has been weighted and the different materials tested do not possess the same densities. The cell diameter is 1cm.

Characterizations

Scanning electron microscopy (SEM) observations were performed with a Hitachi TM-1000 apparatus at 15 kV. The specimens were gold-palladium-coated in a vacuum evaporator prior to examination. High-resolution transmission electron microscopy (HR-TEM) micrographs were obtained with a Jeol 2200 FS microscope. The samples were prepared as followed: carbonaceous powders were deposited on a copper grid coated with a Formvar/carbon membrane. Surface areas and pore characteristics on a micro-(meso)scale were obtained with a Micromeritics ASAP 2010 apparatus. Intrusion/extrusion mercury measurements were performed using a Micromeritics Autopore IV 9500 porosimeter, this to reach the scaffolds macrocellular cells characteristics (with the following parameters: contact angle = 130 °, mercury surface tension = 485 dyne·cm^{-1}, maximum intrusion pressure = 124 MPa). The samples were studied by X-ray diffraction using a Bruker D8 diffractometer (Cu K_α radiation, λ = 1.54056 Å) equipped with a position sensitive detector (PSD). Galvanostatic and potentionstatic cycling measurements are performed with a classical two-electrode Swagelok-type™ cell using 0.1 mL electrolyte with C/10 current densities voltage range between 1.0-3.0 V vs Li with VMP3 (Bio-logic, France). Metallic nanoparticles loadings have been addressed by flame spectrophotometry, so called elemental analyses.

Results and discussion

Open cell carbonaceous materials appear as outstanding candidates for a wide scope of applications ranging from water and air purification, adsorption to electro-catalysis, energy storage and conversion.[11,12] The rational design of such porous carbonaceous materials is thus of first importance and relies either on hard or soft templating synthetic paths where pore morphologies, pore sizes and size distributions are tuned with a certain versatility. The hard template route[13] is based on pre-existing hard porous templates impregnated with a carbon source being subsequently carbonized under non-oxidative atmosphere. After dissolution of the hard template, a negative carbonaceous replica is finally obtained. In this context, we have proposed recently generation of carbonaceous micro-macroporous[10a] and meso-macroporous[10b] monolithic foams using silica-HIPE[9] as exo-templating matrices, HIPE being the acronym for High Internal Phase Emulsion.[14] Using this synthetic path, the carbonaceous foams obtained from the Si-HIPE hard template are in a monolithic shape, bearing open macroporosity with a texture that resembles aggregated hollow spheres, as observed before[14] (**Figure 1**).

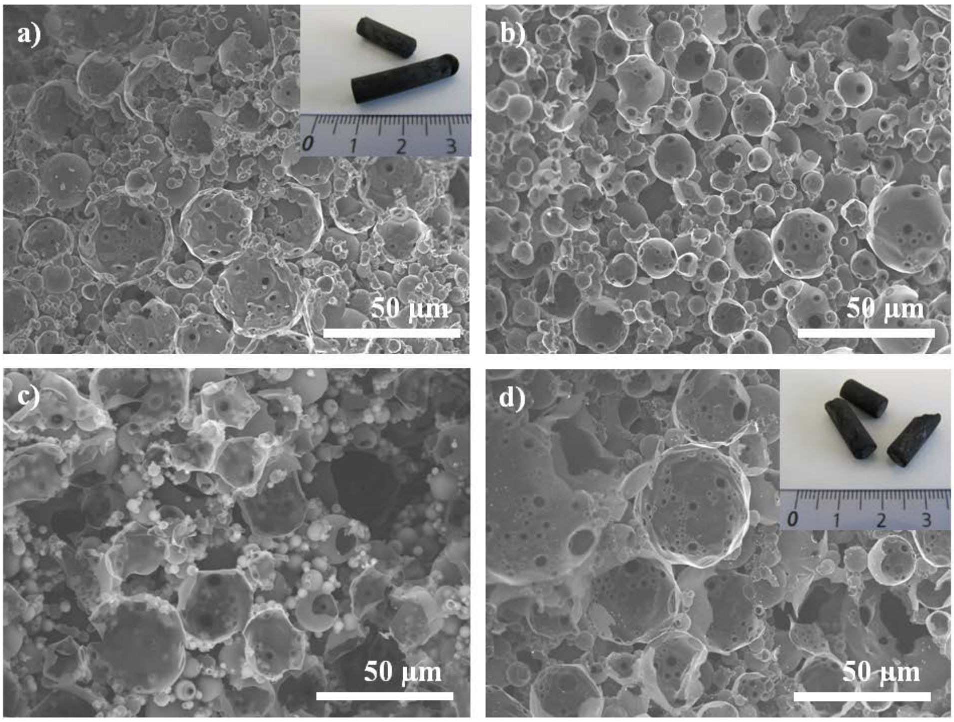

Figure 1. SEM micrographs (secondary electrons detector) of the starting macrocellular carbonaceous foams. a) C-HIPE$_{(80HF)}$, b), C-HIPE$_{(2P5HF)}$ c), C-HIPE$_{(25HF)}$, d) C-HIPE$_{(4F5HF)}$. Embedded: optical photographs showing their monolithic shape.

After infiltration of the metallic salts and their reduction, the Pd and Au particles repartition can be investigated by SEM using a back-scattered electrons detector (**Figure 2**). We observe that this repartition is rather homogeneous, whatever the foam type. Some particle aggregation can be observed for the Pd@C-HIPE$_{(x)}$ and the Au@C-HIPE$_{(x)}$ foams series.

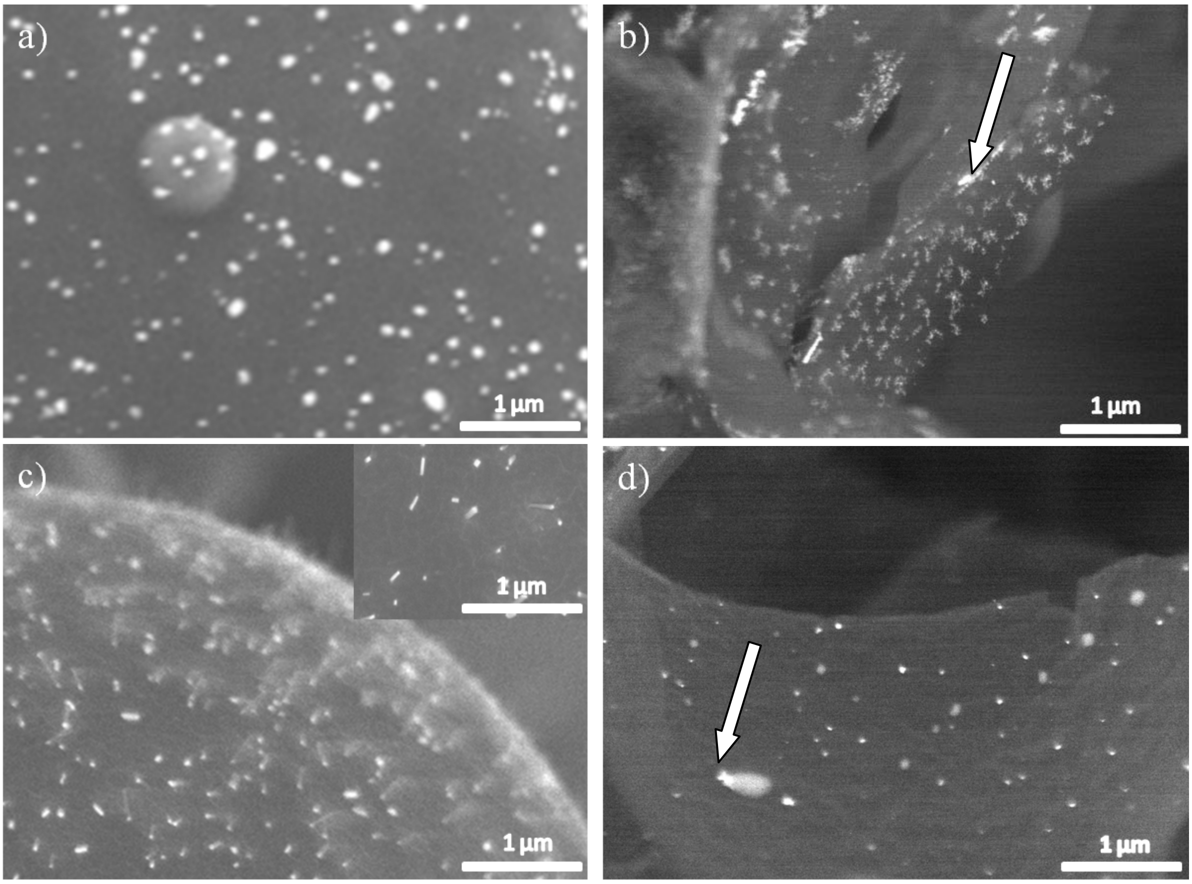

Figure 2. SEM micrographs (back-scattered electrons detector). a) Pd@C-HIPE$_{(25HF)}$, b) Pd@C-HIPE$_{(4P5HF)}$, c) Au@C-HIPE$_{(25HF)}$, d) Au@C-HIPE$_{(4P5HF)}$, white arrow corresponds to an aggregation of metallic particles. The shiny spots correspond to heavy elements area, namely gold and palladium species.

To characterize the metal@C-HIPE$_{(y)}$ foams porosity at the macroscopic length scale mercury porosimetry analyses were performed. Mercury porosimetry assesses the pore diameters that minimize mercury infiltration, i.e. the windows that connect adjacent cells and not the cells themselves. These window diameters distributions are depicted in **Figure 3**. As observed for the Si-HIPE hard templates,[9] the windows size distributions are polydisperse with bimodal contributions.

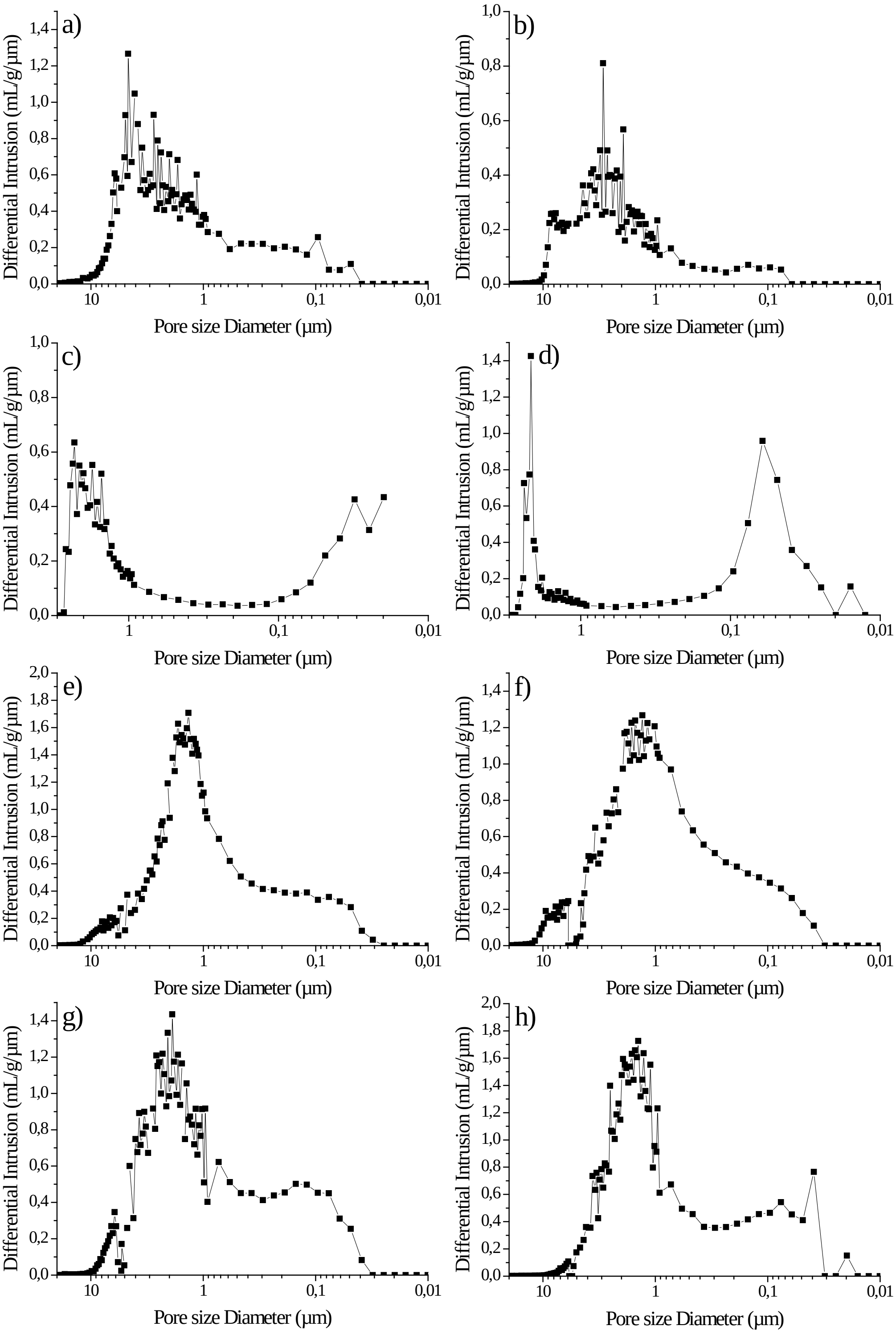

Figure 3. Windows size distributions obtained by mercury porosimetry. a) Pd@C-HIPE$_{(25HF)}$, b) Au@C-HIPE$_{(25HF)}$, c) Pd@C-HIPE$_{(80HF)}$, d) Au@C-HIPE$_{(80HF)}$, e) Pd@C-HIPE$_{(2P5HF)}$, f) Au@C-HIPE$_{(2P5HF)}$, g) Pd@C-HIPE$_{(4F5HF)}$, h) Au@C-HIPE$_{(4F5HF)}$.

As explained before,[9] this feature is induced by the aggregated hollow spheres aspect leading to the coexistence of internal and external cell junctions. We can notice that the bimodal values fall above 1 µm (external junctions) and below 100 nm (internal ones). In addition, mercury porosimetry provides information regarding the foam porosity, as well as bulk density. The mercury porosimetry results are summarized in **Table 1**.

Table 1. Foams macroscopic characteristics obtained from mercury porosimetry.

Materials	Intrusion volume ($cm^3 \cdot g^{-1}$)	Porosity (%)	Bulk density ($g \cdot cm^{-3}$)
Pd@C-HIPE$_{(25HF)}$	4.57	84	0.18
Pd@C-HIPE$_{(80HF)}$	0.76	56	0.74
Pd@C-HIPE$_{(4F5HF)}$	4.76	77	0.16
Pd@C-HIPE$_{(2P5HF)}$	4.68	82	0.17
Au@C-HIPE$_{(25HF)}$	2.43	68	0.28
Au@C-HIPE$_{(80HF)}$	0.62	47	0.76
Au@C-HIPE$_{(4F5HF)}$	4.64	89	0.19
Au@C-HIPE$_{(2P5HF)}$	4.61	83	0.18

Considering **Table 1,** we can see that porosity varies from 50% to 90%, with the lowest value for the metal@C-HIPE$_{(80HF)}$ materials synthesized from the highest amount of phenolic resin, thus filling a good part of the accessible void. The overall porosity falls completely within the range of those of carbonaceous foams obtained previously.[10] The differences emerge from the bulk densities that are slightly higher because these foams now contain heavy metals and residual KCl in the case of the gold-modified carbonaceous foams.

At the mesoscopic length scale, nitrogen physisorption measurements have been carried out (**Figure 4)**. The nitrogen physisorption isotherms can be divided in two sets. The isotherms in **Figure 4a-d**, are of type I-II, corresponding to microporous materials with weak mesoporosity if any. This result was expected as no surfactant was used to create mesoporosity, while microporosity was induced through THF departure when pre-polymerizing the resin by thermal treatment.[10a] The last four isotherms (**Figure 4e-h**) are of type II-IV indicating mesoporosity. If we compare these results to previous foams free of metal,[10b] the decrease in specific surface area certainly comes from the clogging of some accesses to the mesoscopic void spaces by the metal particles. Overall, these foams specific surface areas, extracted either with the BET, BJH or *t*-Plot (when possible) equations, are proposed in **Table 2**.

Table 2. Foams specific surface area obtained from nitrogen physisorption measurements.

	BET ($\mathrm{m^2 \cdot g^{-1}}$)	BJH ($\mathrm{m^2 \cdot g^{-1}}$)	*t*-Plot ($\mathrm{m^2 \cdot g^{-1}}$)	
		Adsorption	External	Meso /Micro
Pd@C-HIPE$_{\mathrm{(80HF)}}$	570		3	567
Au@C-HIPE$_{\mathrm{(80HF)}}$	179		3	175
Pd@C-HIPE$_{\mathrm{(25HF)}}$	606		33	573
Au@C-HIPE$_{\mathrm{(25HF)}}$	122		4	118
Pd@C-HIPE$_{\mathrm{(2P5HF)}}$	285	131	24	261
Au@C-HIPE$_{\mathrm{(2P5HF)}}$	200	91	19	182
Pd@C-HIPE$_{\mathrm{(4F5HF)}}$	157	115	34	123
Au@C-HIPE$_{\mathrm{(4F5HF)}}$	95	46	29	66

For each C-HIPE support, we can notice that the BET surface area is smaller for the Au@C-HIPE$_{(x)}$ series than for the Pd@C-HIPE$_{(x)}$ one. Indeed, SEM micrographs (**Figure 2a,d**) show that the gold particles are smaller than the palladium ones (**Figures 5, 6**) and more homogeneously dispersed at the macropore surface. This feature will probably minimize the nitrogen diffusion through the porosity. In addition, we have characterized the mesoscopic voids organization by small angle X-ray scattering (SAXS) experiments (**Figure S1**). In agreement with the N_2 sorption results and the synthetic path, we notice that the foam series Pd/Au@C-HIPE$_{\mathrm{(25HF)}}$ and Pd/Au@C-HIPE$_{\mathrm{(80HF)}}$ do not present any mesoscopic organization. On the contrary, the series Pd/Au@C-HIPE$_{\mathrm{(4F5HF)}}$ and Pd/Au@C-HIPE$_{\mathrm{(2P5HF)}}$, obtained using lyotropic mesophases, exhibit vermicular organization with a single diffraction peak at the wave vector q = 0.057 Å^{-1} ($d_{\mathrm{spacing}}=2\pi/q$), less pronounced for the Pd/Au@C-HIPE$_{\mathrm{(2P5HF)}}$ hybrid foam series

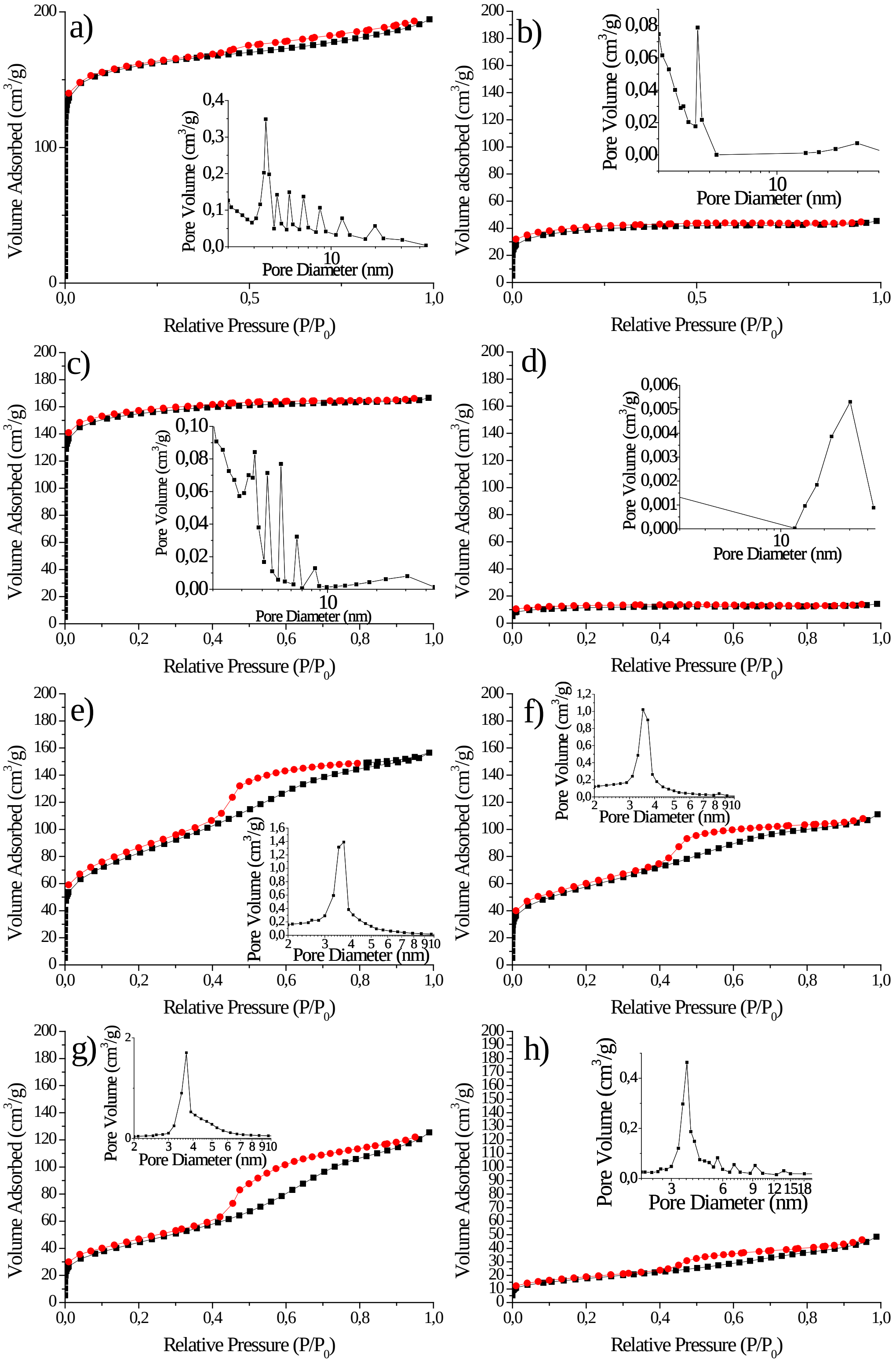

Figure 4. Nitrogen sorption/desorption isotherms. a) Pd@C-HIPE$_{(25HF)}$, b) Au@C-HIPE$_{(25HF)}$, c) Pd@C-HIPE$_{(80HF)}$, d) Au@C-HIPE$_{(80HF)}$, e) Pd@C-HIPE$_{(2P5HF)}$, f) Au@C-HIPE$_{(2P5HF)}$, g) Pd@C-HIPE$_{(4F5HF)}$, h) Au@C-HIPE$_{(4F5HF)}$.

Considering **Figure 5b,d,f,h,** we can notice that the particles are polycrystalline as grain boundaries can be easily seen. On **Figure 5a,c,e,g,** it is obvious that the particle size distributions are rather polydisperse.

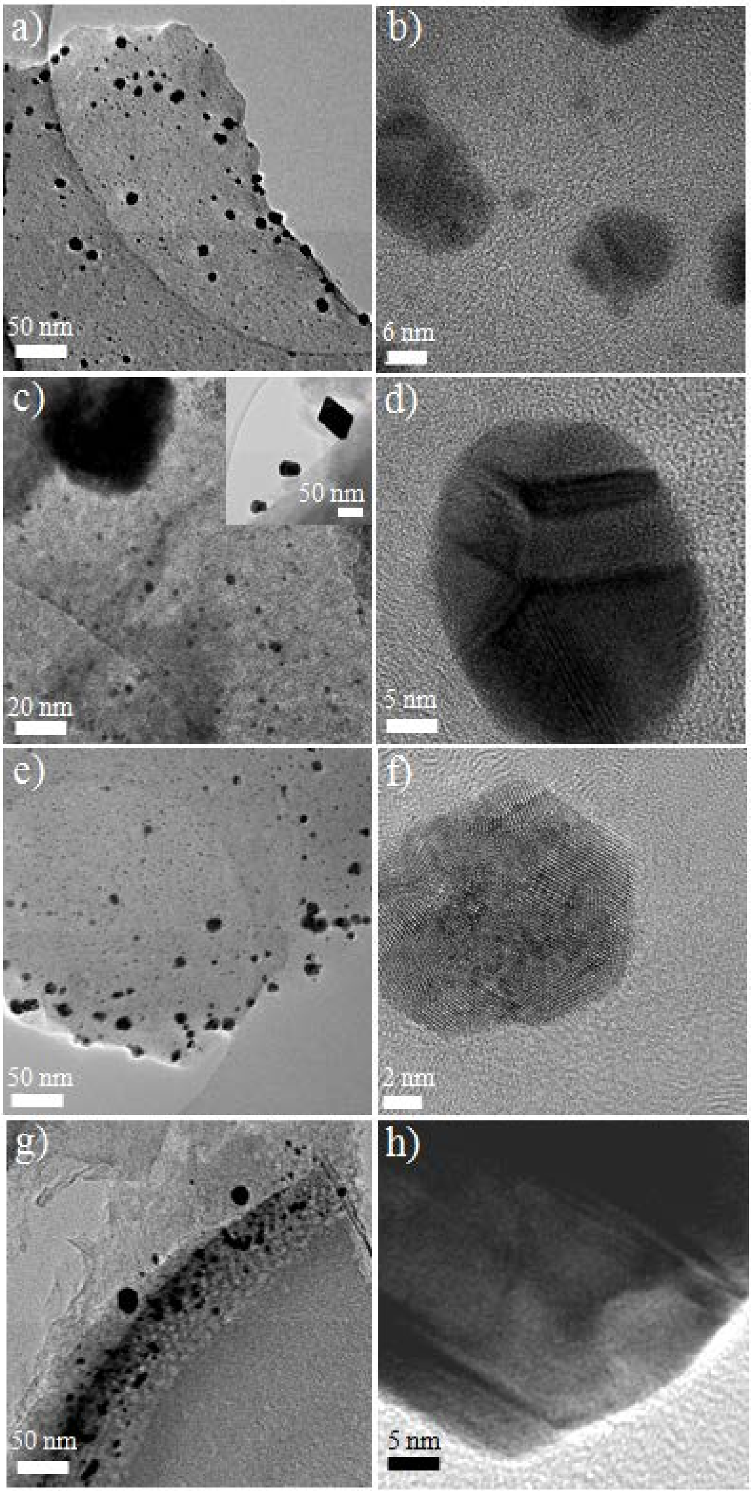

Figure 5. HR-TEM micrographs. a-b) Pd@C-HIPE$_{(25HF)}$ c-d) Au@C-HIPE$_{(25HF)}$, e-f) Pd@C-HIPE$_{(4F5HF)}$, g-h) Au@C-HIPE$_{(4F5HF)}$.

In order to get better quantitative results, several TEM and HR-TEM micrographs were mathematically analyzed to roughly estimate the distributions of particles diameters. The results are shown in **Figure 6.**

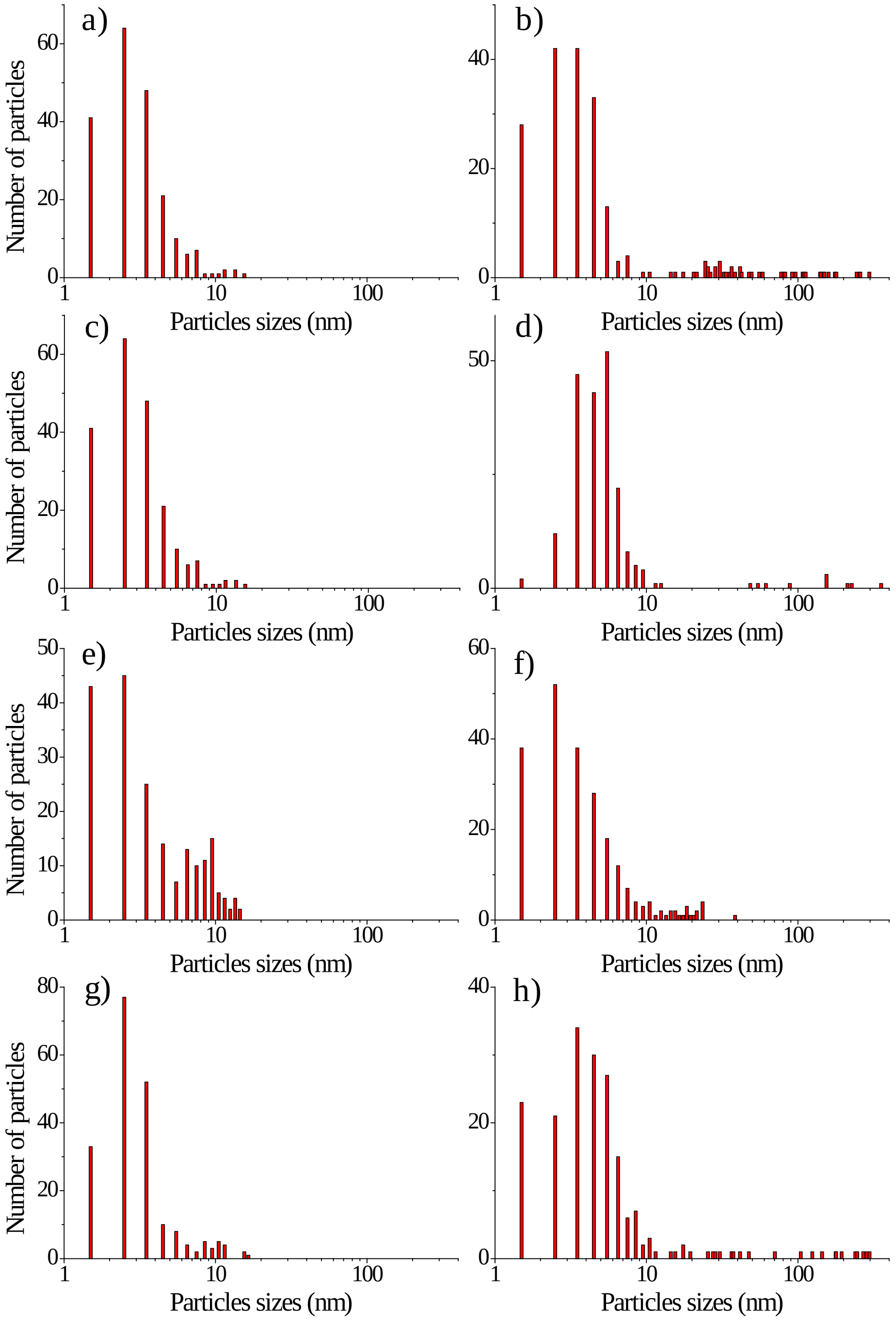

Figure 6. Populations of particle diameters obtained by analyzing both TEM and HR-TEM images. The histograms have been constructed by scanning 2 µm^2 of each sample. a) Pd@C-HIPE$_{(25HF)}$, b) Au@C-HIPE$_{(25HF)}$, c) Pd@C-HIPE$_{(80HF)}$, d) Au@C-HIPE$_{(80HF)}$, e) Pd@C-HIPE$_{(2P5HF)}$, f) Au@C-HIPE$_{(2P5HF)}$, g) Pd@C-HIPE$_{(4F5HF)}$, h) Au@C-HIPE$_{(4F5HF)}$.

We can note the polydisperse character of the particle diameters, whatever the metal used or the type of porosity. These broad distributions indicate that heterogeneous nucleation took place both inside the mesopores, when mesopores are present, and also at the macropores surface, leading to the higher particle diameters as revealed with the HR-TEM visualization of **Figure 5**. We can also notice that some gold nanoparticles have diameters above 20 nm in all the foams containing gold, which is never the case for the Pd loaded foams whatever the micoporous-mesoporous balance. Quantitatively, the amount of metal loading within the metal@C-HIPE$_{(x)}$ foams has been assessed by elemental analysis. The results obtained are summarized in **Table 3**. The Au wt% is always higher than the Pd wt% for the same porosity. Indeed, the metal loading has to be compared with the starting concentration of phenolic resin used to synthesize the foams: 25 wt % (25HF), 80 wt % (80HF), 21 wt % (4F5HF), 23 wt % (2P5HF). We thus notice that the amount of metal is inversely proportional to the starting amount of the carbonaceous precursor. This feature is thereby expected as the metal wt% is relative to the amount of carbon.

Table 3. Foams' metal loading obtained from elemental analysis (wt %).

Materials	Pd	Au
Pd@C-HIPE$_{(25HF)}$	8.15	
Pd@C-HIPE$_{(80HF)}$	0.9	
Pd@C-HIPE$_{(4F5HF)}$	2.89	
Pd@C-HIPE$_{(2P5HF)}$	4.24	
Au@C-HIPE$_{(25HF)}$		10.07
Au@C-HIPE$_{(80HF)}$		4.56
Au@C-HIPE$_{(4F5HF)}$		8.81
Au@C-HIPE$_{(2P5HF)}$		9.79

The next issue is the characterization of the particle structures and zerovalent state. The particles metallic state has been first investigated through XPS experiments, and the results are proposed in **Figure 7**. Typical XPS survey spectra are presented in **Figure 7a,b**. We can notice that the foams have in common the presence of carbon and oxygen. The presence of oxygen is expected as we have demonstrated recently[10b] that from the same source of carbon, the deconvolution of the C1s peak around 280-295 eV shows the presence of COOH, COOR, C=O and C-O heterofunctions at the foams' walls surface.

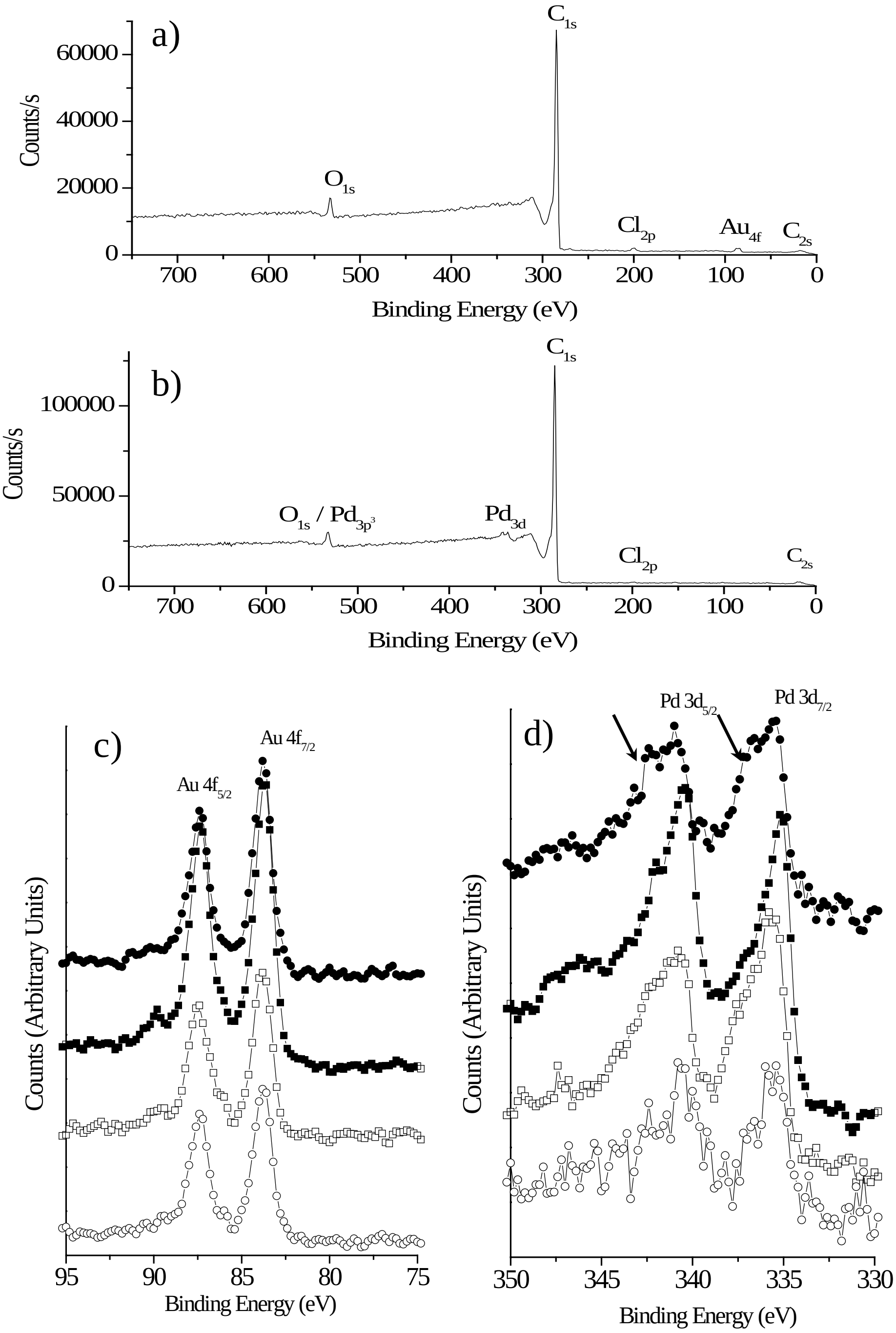

Figure 7. XPS investigations. Example of XPS survey acquisition for: a) Au@C-HIPE$_{(2P5HF)}$ foam, and b) Pd@C-HIPE$_{(2P5HF)}$ foam; XPS spectra focused on: c) the Au binding energies, and d) the Pd binding energies; ● Au/Pd@C-HIPE$_{(2P5HF)}$, ○ Au/Pd@C-HIPE$_{(80HF)}$, □

Au/Pd@C-HIPE$_{(4F5HF)}$, ■ Au/Pd@C-HIPE$_{(25HF)}$. The black arrows in d) indicate the PdO (Pd 3d$_{7/2}$ and Pd 3d$_{5/2}$) peaks.

XPS spectra of the Au/Pd@carbon(HIPE)x series differ when focusing on the binding energies of Au and Pd. In **Figure 7c** the Au 4f$_{7/2}$ and 4f$_{5/2}$ peaks at 83.6 and 87.5 eV respectively demonstrate without ambiguity the full reduction of the gold salt into zerovalent metallic particles.[15] The palladium oxidation state is addressed in the **Figure 7d**. The XPS spectrum shows the Pd 3d$_{3/2}$ and Pd 3d$_{5/2}$ peaks of metallic zerovalent Pd respectively at 340.3 eV and 335.5 eV. Shoulders on both peaks at higher binding energy values can be attributed to palladium oxide PdO.[15a,16] This characteristic demonstrates that Pd^0 particles are partially covered with PdO. We have earlier established that when 1-2 nm of the material surface was dug with an electron beam, a shift of those peaks is observed towards characteristic metallic Pd 3d$_{5/2}$ and 3d$_{7/2}$ peaks.[15b] Basically, partial oxidation of Pd particles surface is always observed when specific stabilizers as triphenylphosphine or mercapto groups are not employed.[17] Beyond their zerovalent or oxide nature, the structures of the embedded particles have been assessed with XRD (**Figure 8**). Considering **Figure 8a,** the Au@C-HIPE$_{(x)}$ foam series diffraction patterns display the characteristics Bragg diffractions of *cfc* gold in the range 30-70 2θ. This feature is in agreement with the XPS results considering the zerovalent state of the Au particles nucleated within these carbonaceous foams. On **Figure 8b**, dedicated to the XRD for the palladium foams series, we can notice that the behavior is not the same, except for the Pd@C-HIPE$_{(25HF)}$ foam where the three main Bragg diffraction peaks of *cfc* Pd are present without ambiguity within the range 30-70 2θ. In addition, for the whole Pd@C-HIPE$_{(x)}$ foam series there is no evident sign of crystalline palladium oxide species, meaning that oxidized palladium species are not highly concentrated and small enough not to provide detectable XRD patterns. When considering the diffraction patterns for the Pd@C-HIPE$_{(2P5HF)}$, Pd@C-HIPE$_{(80HF)}$, and Pd@C-HIPE$_{(4F5HF)}$ foams, we can notice that the diffraction peaks are broadened, which means that the palladium is either poorly crystalline or that the particles we observe are mainly a shell of palladium oxide containing a small core of palladium (**Fig. 7** XPS) and not highly concentrated within the foams core. In correlation with the elemental analysis results (**Table 3**), the broader the diffraction peaks, the lower the Pd loading within these foams.

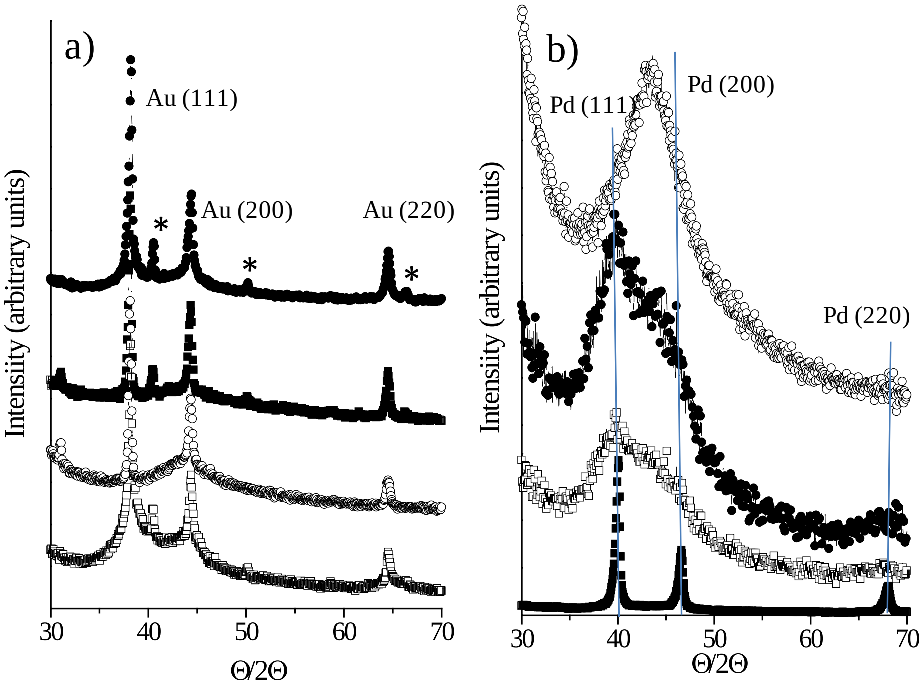

Figure 8. Hybrid foams X-ray diffractograms. a) ● Au@C-HIPE$_{(2P5HF)}$, ○ Au@C-HIPE$_{(80HF)}$, ☐ Au@C-HIPE$_{(4F5HF)}$, ■ Au@C-HIPE$_{(25HF)}$; b) ● Pd@C-HIPE$_{(2P5HF)}$, ○ Pd@C-HIPE$_{(80HF)}$, ☐ Pd@C-HIPE$_{(4F5HF)}$, ■ Pd@C-HIPE$_{(25HF)}$. The stars in Figure a) indicate from left to right the KCl (202), (222) and (420) diffraction peaks.

The electrochemical cycling of the different carbon Au/Pd@foams are shown in Figure 9. At first glance the results are quite deceiving when compared with the C-HIPE$_{(2P5HF)}$ free of metallic loading, for which 2 Lithium are exchanged without any optimization of the C-HIPE$_{(2P5HF)}$ electrode, a result close to the theoretical capacity (Figure S2). Here we can see that the number of Li exchanged vary from below 0.5 Li (Pd@C-HIPE$_{(80HF)}$) to 1.5 Li (Pd@C-HIPE$_{(4F5HF)}$) at best. We can also notice that the capacity losses increase with the number of exchanged Li especially when the number of Li is closed to 1.5 Li that may be linked to the formation of insulated Li_2S species.

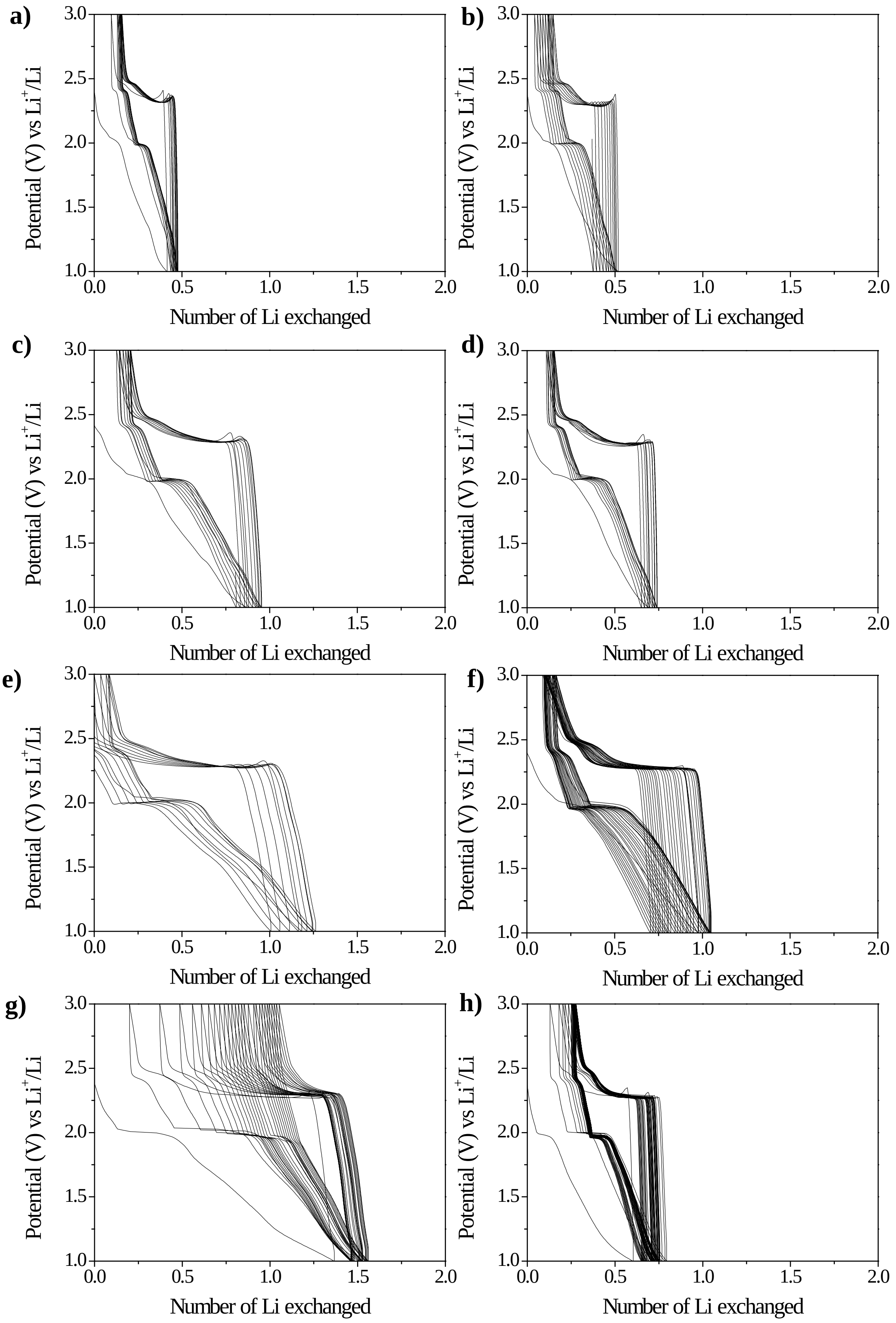

Figure 9. Cycling performances of the materials. a) Pd@C-HIPE$_{(80HF)}$, b) Au@C-HIPE$_{(80HF)}$, c) Pd@C-HIPE$_{(25HF)}$, d) Au@C-HIPE$_{(25HF)}$, e) Pd@C-HIPE$_{(2P5HF)}$, f) Au@C-HIPE$_{(2P5HF)}$, g) Pd@C-HIPE$_{(4F5HF)}$, h) Au@C-HIPE$_{(4F5HF)}$.

This effect of formation of insulated Li2S is also observable on **Figure 10a** that depicts the metal loaded carbonaceous foams gravimetric capacity versus the number of cycles and Figure 10b without metal loadings. Overall, A better capacity retention is obtained when the initial capacity is low.

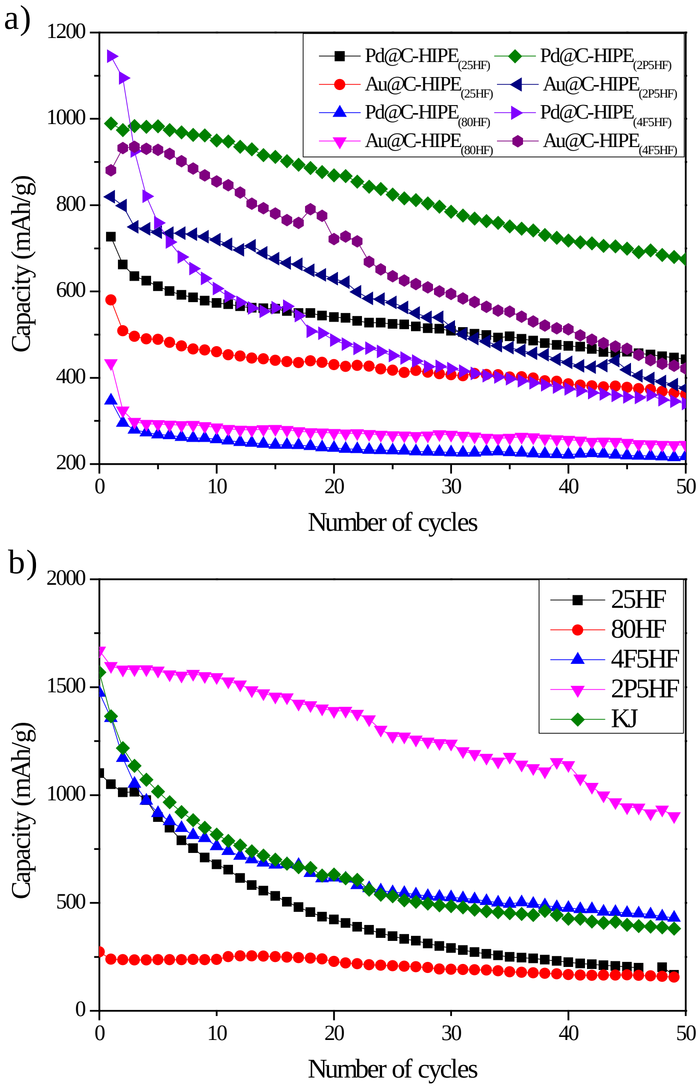

Figure 10. Capacities over number of cycles for various C- Metal composites a) and b) carbonaceous foams free of metallic nanoparticles, extracted from reference 7.

On the one hand, considering Figure **9a,c,e,g** and the Pd@C-(HIPE) foam series, we can see that the capacity loss increases with mesoporosity (**Table 2**) whatever the wt% of Pd loaded. On the other hand, the number of Li exchanged increases with the mesoporosity. This result is consistent with what is observed without metal,[7] where good cycling performances come from balanced mesoscopic surface and bulk density. With this Pd loaded foam series, we can state that the Pd loading is not the parameter that governs both the first discharged capacity and the remnant capacity after several cycles (**Figure 10a, Table 4**). This is certainly due to a lack of chemical affinity between the sulfur atoms of polysulfides and the slightly oxidized Pd nanoparticles surface (**Figure 7**). As a direct consequence, **Figure 10a** shows that the capacity after the first discharge is by far lower for the foams without mesoporosity (25HF and 80HF) compared to those with mesoporosity (2P5HF and 4F5HF). The Pd –based system showing both the highest capacity and stability when cycling is the Pd@C-HIPE$_{(2P5HF)}$. The effect of gold loading on polysulfides leaching is obvious. For instance on **Figure 9,b,d,f,h** we can see that the number of Li exchanged fall between 0.5 and 1 with good capacity retention (Fig. 10a) whatever the gold loading, mesoporosity and bulk density. The adjunction of gold nanoparticles tends to stabilize the anchoring of polysulfides at the cathodes. This effect was expected due to the great affinity of gold surface with sulfur atoms, which localizes the nucleation and growth of lithium polysulfide intermediates. At that stage, we can say that the effect of metal loading within the carbonaceous foams is somewhat deceiving: as much as we minimized the polysulfides leaching effect when cycling with gold nanoparticles addition, we simultaneously minimized both the starting and capacity upon cycling compared to foams free of gold nanoparticles (**Figure 10b**) because the nanoparticles block the mesoporosity. For the palladium adjunction, its effect is worse as the Pd-sulfides affinity does not compensate the lack of surface area. On the other hand, the story is not the same when considering the volumic expression of capacity (**Table 4**).

In a previous study[7] we have claimed that in order to really assess the electrodes power efficiency, dealing with foams and voids, it is of crucial importance to provide the capacities not only normalized per gram of active material but also per volume. The capacities with the dimensionalities mA.h.g^{-1} and mA.h.cm^{-3},[7] are summarized in **Table 4**. This table reveals the importance of considering the capacities in mA.h.cm^{-3} in order to appreciate the effect of metal loading within those carbonaceous foams. Considering the Pd loaded series, the results are almost the same whatever the Pd loading, as its effect is almost negligible both for the starting and remnant capacities after 50 cycles.

Table 4. Materials starting capacity and after 50 cycles expressed both per mass and per volume. The volumic capacities are obtained when multiplying the mass capacities per the foams bulk densities provided within the Table 1.* Capacity values of the carbonaceous foams without loading of metallic nanoparticles, values extracted from ref 7.

Materials	Starting capacity (mA h g^{-1})	Starting capacity (mA h cm^{-3})	Remnant capacity after 50 cycles (mA h g^{-1})	Remnant capacity after 50 cycles (mA h cm^{-3})
Pd@C-HIPE$_{(25HF)}$	725	131	450	81
Au@C-HIPE$_{(25HF)}$	587	164	370	104
Pd@C-HIPE$_{(80HF)}$	350	263	210	158
Au@C-HIPE$_{(80HF)}$	430	327	240	182
Pd@C-HIPE$_{(2P5HF)}$	1000	170	680	116
Au@C-HIPE$_{(2P5HF)}$	810	146	380	68
Pd@C-HIPE$_{(4F5HF)}$	1150	184	360	58
Au@C-HIPE$_{(4F5HF)}$	890	160	420	76
*C-HIPE$_{(25HF)}$	1120	168	165	23
*C-HIPE$_{(80HF)}$	250	175	165	115
*C-HIPE$_{(2P5HF)}$	1680	202	1000	150
*C-HIPE$_{(4F5HF)}$	1500	225	430	52

We have to underline that the Pd@C-HIPE$_{(80HF)}$ material presents higher volumic and weight capacities (both after the first discharge and after 50 cycles) than its homologous C-HIPE$_{(80HF)}$ foam free of metals. Considering the gold loaded carbonaceous foams, and at the exception of the foam Au@C-HIPE$_{(80HF)}$, we can see that the starting weight capacities, after first discharge and the remnant ones after 50 cycles are smaller than the analogous foams free of metals. But when considering the volumic capacities, we can see that the Au@C-HIPE$_{(80HF)}$ foam is providing better efficiency at the first discharge (327 mA.h.cm$^{-3)}$, and after 50 cycles

(182 mA.h.cm^{-3}) when compared to the best foam free of metal loading namely the C-HIPE$_{(2P5HF)}$ which exhibits 202 mA.h.cm^{-3} for the first discharge and 150 mA.h.cm^{-3}after 50 cycles. It means that for the Au@C-HIPE$_{(80HF),}$ the presence of gold compensates the lack of mesoporosity. As such the Au@C-HIPE$_{(80HF)}$ retains 63% of restituted weight and volumic capacity after 50 cycles, compared to 60% for the C-HIPE$_{(2P5HF)}$ foam. Thus, the introduction of metal, particularly gold nanoparticles, is of importance for providing stability of LiS-based electrodes when cycling. Here again, we evidence the importance of providing capacities both in mA.h.g^{-1} and mA.h.cm^{-3} to really address the effect of parameters such as porosity, surface area and wt% of metal loaded.

Conclusion

Macrocellular carbonaceous foams containing metallic nanoparticle of Pd/Au have been synthesized and used to confine polysulfides at the cathode of Li-S batteries. The multiplex synthetic pathway is typical of integrative chemistry,[19] involving emulsions, sol-gel chemistry, exotemplating and nanoparticles nucleation to obtain metal-loaded carbon monoliths bearing hierarchical porosity. This work extends our first experiments with Li-S batteries, where we explored the influence of porosity in carbonaceous monoliths on capacity and cycling performances.[7] We now have demonstrated that noble metal nanoparticles are an interesting way to enhance the properties of our materials thanks to the surface chemistry of Au and Pd, as shown with the Au@C-HIPE$_{(80HF)}$ sample which exhibits a starting capacity of 327 mA.h.cm^{-3}, compared to 175 mA.h.cm^{-3} without Au nanoparticles. The remnant capacity after 50 cycles also has been enhanced.

This Au@C-HIPE$_{(80HF)}$ sample is one of the less interesting sample in term of power density per mass with 430 mA.h.g^{-1}, but the most interesting one in terms of power density per volume with 327 mA.h.cm^{-3}. The best sample in terms of power density per mass remains the previously synthesis C-HIPE$_{(2P5HF)}$ with 202 mA.h.cm^{-3} and 1680 mA.h.g^{-1} respectively. It shows again the importance of quantifying the capacity not only by weight (mA.h.g^{-1}) but also by volume (mA.h.cm^{-3}). Volume is indeed an important parameter to consider, depending whether applications focus on power density per volume or per mass. It also allows accounting for the fact that as we are dealing with porous materials, some results come more from a low density than an actual improvement in the intrinsic interfacial chemistry (energy conversion) of the material. The importance of metallic nanoparticles, Au in particular, for the stability of carbon-based electrodes during Li-S batteries cycling has been demonstrated. Future work will focus on studying the effects of different loadings on the performances of these materials.

References

1 Armand, M.; Tarascon, J.M. *Nature* **2008**, *451*, 652-657

2 Agostini, M.; Aihara, Y.; Yamada, T.; Scrosati, B.; Hassoun, J. *Solid State Ionics* **2013**, *224*, 48-51

3 (a) Akridge, J.R.; Mikhaylik, Y.V.; White, N. *Solid State Ionics* **2004**, 175, 243.

(b) Cheon, S.E.; Choi, S.S.; Han, J.S.; Choi, Y.S.; Jung, B.H.; Lim, H.S. *J. Electrochem. Soc.* **2004**, 151, A2067

(c) Yamin, H.; Gorenshtein, A.; Penciner, J.; Sternberg, Y.; Peled, E. *J. Electrochem. Soc.* **1988**, 135, 1045

(d) Kang, K.; Meng, Y.S.; Breger, J.; Grey, C.P.; Ceder, G. *Science* **2006**, 311, 977

4 (a) Herbert, D.; Ulam, J. *US pat. N° 3043896*, **1962.** (b) Elazari, R.; Salitra, G.; Taylosef, Y.; Grinblat, J.; Scordilis-kellay, C.; Xiao, A.; Affinito, J.; Aurbach, D. *J. Electrochem. Soc.* **2010**, 157, A1131

5 (a) Ji, X.; Lee, K.T.; Nazar, L. F. *Nature Mater.* **2009**, 8, 500.(b) Wang, H.; Yang, Y.; Liang, Y.; Robinson, J.T.; Li, Y.; Jackson, A.; Gui, Y.; Dai, Y. *Nanolett.* **2011**, 2644. (c) Evers, S.; Yim, T.; Nazar, L. F. *J. Phys. Chem. C* **2012**, 116, 19653.

6 Demir-Cakan, R.; Morcrette, M.; Guéguen, A.; Dedryvère, R.; Tarascon, J.-M. *Energy Environ. Sci*. **2013**, *6*, 176.

7 Depardieu, M.; Janot, R.; Sanchez, C.; Bentaleb, A.; Gervais, C.; Birot, M.; Demir-Cakan, R.; Backov, R.; Morcrette, M. *RSC Advances* **2014**, *4*, 23971-23976.

8 Depardieu, M.; Janot, R. Sanchez, C.; Deleuze, H.; Morcrette, M.; Gervais, C.; Backov, R. *J. Mat. Chem A* **2014, 2,** 7694-7701.

9 Carn, F.; Colin, A.; Achard, M.-F.; Deleuze, H.; Birot, M.; Backov, R. *J. Mater. Chem.* **2004**, 14, 1370

10 *(a)* Brun, N.; Prabaharan, S.R.S.; Morcrette, M.; Sanchez, C.; Pécastaing, G.; Derré, A.; Soum, A.; Deleuze, H.; Birot, M.; Backov, R. *Adv. Funct. Mater*, **2009**, *19*, 3136. *(b)* Brun, N.; Prabaharan, S.R.S.; Morcrette, M.; Deleuze, H.; Birot, M.; Babot, O.; Achard, M.-F.; Surcin, C.; Backov, R. *J. Phys. Chem. C*, **2012**, *116*, 1408

11 Foley, H.C. *Microporous Mater*. **1995**, *4*, 407.

12 Kyotani, T. *Carbon* **2000**, 38, 269.

13 Schüth, F. *Angew. Chem. Int. Ed*. **2003**, *42*, 3604.

14 (a) Barby, D.; Haq, Z. *Eur. Pat. 0060138*, **1982** (b) Cameron, N.R.; Sherrington, D.C. High Internal Phase Emulsions (HIPEs) Structure, properties and use in polymer preparation in *Advances in Polymer Science*, Eds Springer Berlin / Heidelberg, **1996**, 126, 163. (b) Cameron, N. *Polymer* **2005**, 46, 1439 (c) Zhang, H.; Cooper, A.I. *Soft Matter* **2005**, 2, 107

15 *(a)* Brun, M.; Berthet, A.; Bertolini, J. C. *J. Electron Microsc. Relat. Phenom.* **1999**, *104*, 55 (b) Desforges, A.; Deleuze, H.; Mondain-Monval, O.; Backov, R. *Ind. Eng. Chem. Res.* **2005**, *44*, 8521.

16 Tunc, I.; Suzer, S. *J. Phys. Chem. B* **2005**, *109*, 7597.

18 (*a*) Wang, P. H.; Pan, C.-Y. *Colloid Polym. Sci.* **2001**, *279*, 171. (*b*) Desforges, A.; Backov, R.; Deleuze, H.; Mondain-Monval, O. *Adv. Funct. Mat*. **2005**, *15*, 1689.

19 (*a*) Backov, R. *Soft Mater* 2006, *2*, 452. (*b*) Brun, N.; Ungureanu, S.; Deleuze, H.; Backov, R.; *Chem. Soc. Rev*., 2011, 40 , 771. (*c*) Sanchez, C.; Belleville, P.; Popall, M.; Nicole, L. *Chem. Soc. Rev*. 2011, 40, 696.